Soft Matter

ROYAL SOCIETY OF CHEMISTRY

PAPER

View Article Online
View Journal | View Issue

Cite this: *Soft Matter*, 2023, **19**, 6978

Optomechanical computing in liquid crystal elastomers†

Haley M. Tholen, *[a] Cedric P. Ambulo,[bc] Kyung Min Lee,[bc] Philip R. Buskohl[b] and Ryan L. Harne *[a]

Received 22nd June 2023,
Accepted 29th August 2023

DOI: 10.1039/d3sm00819c

rsc.li/soft-matter-journal

Embodied decision-making in soft, engineered matter has sparked recent interest towards the development of intelligent materials. Such decision-making capabilities can be realized in soft materials *via* digital information processing with combinational logic operations. Although previous research has explored soft material actuators and embedded logic in soft materials, achieving a high degree of autonomy in these material systems remains a challenge. Light is an ideal stimulus to trigger information processing in soft materials due to its low thermal effect and remote use. Thus, one approach for developing soft, autonomous materials is to integrate optomechanical computing capabilities in photoresponsive materials. Here, we establish a methodology to embed combinational logic circuitry in a photoresponsive liquid crystal elastomer (LCE) film. These LCEs are designed with embedded switches and integrated circuitry using liquid metal-based conductive traces. The resulting optomechanical computing LCEs can effectively process optical information *via* light, thermal, and mechanical energy conversion. The methods introduced in this work to fabricate a material capable of optical information processing can facilitate the implementation of a sense of sight in soft robotic systems and other compliant devices.

1. Introduction

The integration of sensory awareness and information processing capabilities in compliant, untethered devices is a significant step towards autonomous, intelligent material systems.[1–3] Information processing devices realized in soft matter are desirable for the sake of unique mechanical and optical properties not found in traditional solid-state materials.[4] Soft materials with embedded computing also offer the potential for realization at a molecular scale.[5,6] Furthermore, the development of alternative computing paradigms, such as neuromorphic computing[7] and quantum computing,[8] is piquing the interest of researchers as the limits of conventional electronics are approached. While not all alternative computing techniques may compete with the speed of electronic computing, these systems are still worth exploring to achieve fabrication of standalone material systems with embedded intelligence that require low levels of energy input for operation and deformability.[9–11] Such attributes are beneficial for use in challenging environments in which a compliant information processing device more sophisticated than a sensor is required.

One such approach to incorporate information processing in materials is through combinational logic. Composed of fundamental logic gates, combinational logic has been manifested through mechanical,[12] pneumatic-,[13] thermal-,[14,15] chemical-,[16] and light-based signals.[17] On the other hand, the information processing capabilities in these materials remain largely in their infancy.[18,19] Many examples of soft materials with embedded logic are 2-bit logic gates, because demonstrating the scalability of *n*-bit architectures presents a significant challenge. Combinational logic-based integrated circuits have been shown within a soft material using mechanical stimuli, requiring physical contact with the computing material for operation.[20] While this prior work addresses the networking issues in mechanical logic implementations, the strict limitation to mechanical inputs does not suggest a means to accommodate other sensory stimuli.

Light is an attractive method to control information processing devices since light enables remote and precise actuation. In particular, considering sunlight as a light source enables the development of soft, autonomous materials capable of operating in conditions where electrical power is unavailable. Furthermore, designing a photoresponsive soft material enables actuation based on various intensities, wavelengths, or patterns of light that can be employed for a broad range of applications.

[a] *Department of Mechanical Engineering, The Pennsylvania State University, University Park, PA, USA. E-mail: hmt5321@psu.edu, ryanharne@psu.edu*
[b] *Materials and Manufacturing Directorate, Air Force Research Laboratory, Wright-Patterson Air Force Base, OH, USA*
[c] *Azimuth Corporation, Fairborn, OH, USA*

† Electronic supplementary information (ESI) available. See DOI: https://doi.org/10.1039/d3sm00819c

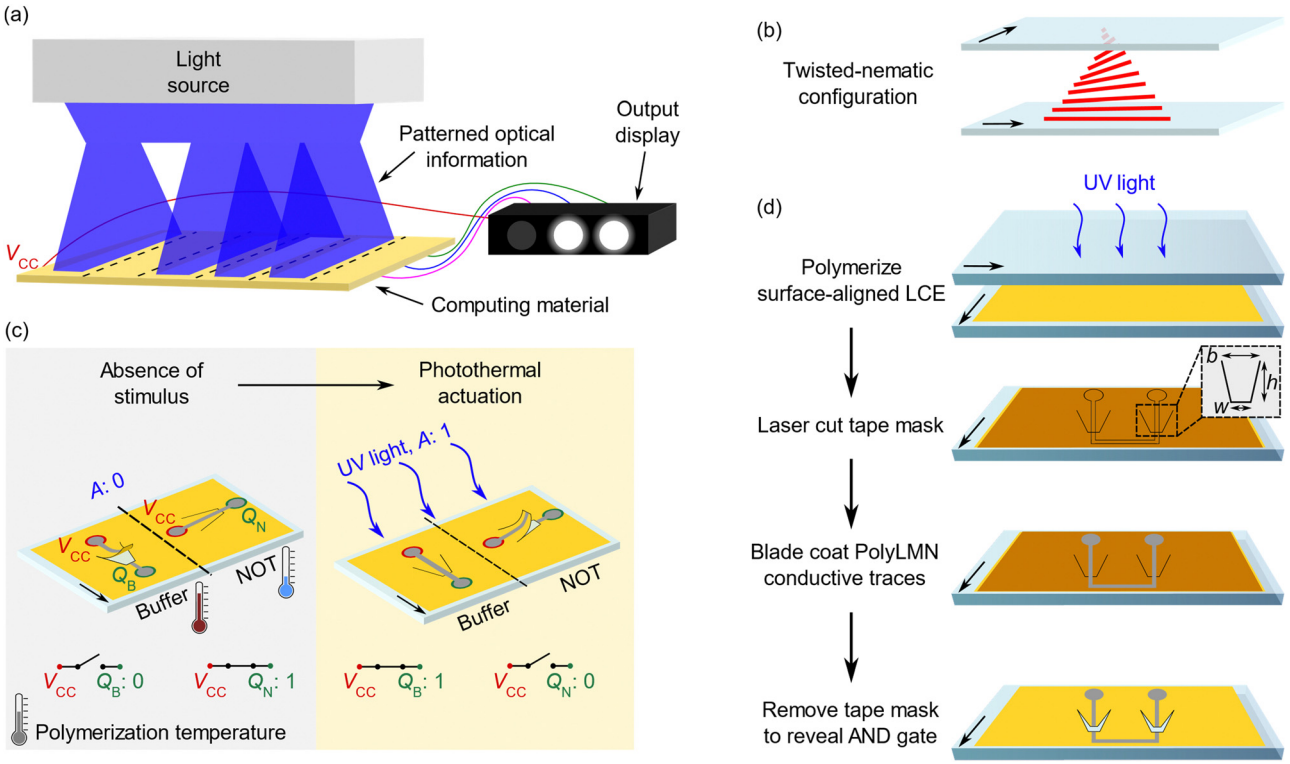

Fig. 1 (a) Concept of computing material that receives digitized optical information and processes the information into new digital signals. (b) Schematic represents twisted-nematic order of liquid crystals, which is responsible for the curling behavior of the LCEs. (c) Schematic to describe working principle of Buffer and NOT switches. The digital optical input, *A*, is determined 0 or 1 based on the optical stimulus being off or on, respectively. The V_{CC} terminal is electrically connected to digital outputs Q_B and Q_N to observe the output signal. Thermometer indicates difference in polymerization temperature to achieve the two types of switches. (d) Fabrication procedure to integrate logic gates in LCEs. Switch geometry is defined with width, base, and height dimensions at w = 1.2 mm, b = 3.5 mm, h = 3.75 mm, respectively.

Such future avenues introduce optomechanical computing capabilities in materials that could be used for environmental health monitoring,[1] heliotropic solar systems,[21] or even a rudimentary form of eyesight in soft robotic systems.[22,23] Optomechanical computing within soft materials also offers significant advantages over conventional mechanical computers in regard to friction and wear. Notably, the performance and longevity of mechanical devices such as MEMS often undergo failures due to friction of surfaces in contact.[24] To date, optically-based information processing in soft materials has been largely limited to small-scale logic operations on the molecular scale,[25,26] despite the benefits of developing soft materials with optical computing capabilities.

In this work, we demonstrate a photoresponsive liquid crystal elastomer (LCE) capable of receiving and processing optical information to introduce a sense of sight in soft, autonomous engineered matter, Fig. 1(a). Optomechanical computing LCEs are designed with embedded switches and integrated circuitry using liquid metal-based conductive traces. LCEs are innately thermotropic: in other words, the orientational order of the liquid crystals is temperature-dependent.[27–29] Further, liquid crystals naturally self-organize along a patterned director (nematic phase) and become disordered as the system is heated.[1,30,31] In addition to an order–disorder transition, liquid crystals exhibit anisotropic coefficients of thermal expansion (CTE) that also contribute to reversible shape change on a macroscopic level.[32,33] The LCEs in this work exhibit twisted-nematic molecular order, meaning the nematic director rotates 90° throughout the thickness of the film, Fig. 1(b). The twisted-nematic switches curl and uncurl with exposure to ultraviolet (UV) light to disconnect and connect conductive traces, respectively, as shown in Fig. 1(c). Photoresponse can be achieved *via* photochemical or photothermal effects.[34,35] To take advantage of the aforementioned temperature-responsive properties of LCEs, the photothermal effect is leveraged in this work. Here, we demonstrate a purely soft, optically actuated material system capable of mechanical computation, contributing to the development of intelligent materials that emulate biological senses, thought processes, and adaptability.

2. Materials and methods

2.1. Cell preparation

Glass cells used for LCE fabrication are composed of glass tiles cut to the desired size of the LCE. For AND and NAND logic gates, standard 1 mm thick microscope slides (Globe Scientific Inc.) are cut in half to 25 × 37.5 mm. Computing LCEs such as the 2-bit adder that require a larger surface area use 1.75 mm thick craft glass tiles (Darice) cut in half to 101.6 × 50.8 mm.

The glass pieces are individually cleaned with acetone and methanol to remove any dust. Glass pieces are then treated with air plasma (Harrick Plasma PDC-32G) for 3 min to remove organic contaminants and make the glass surfaces more hydrophilic. The glass pieces are then spin-coated (SPS SPIN150) with 50 μL of 0.125 wt% Elvamide (DuPont) methanol solution at 2000 rpm and 500 rpm s^{-1} for 20 s. The coated side of each glass piece is rubbed with a velvet cloth to create an alignment layer. Two rubbed glass pieces with orthogonal alignment layers enable the liquid crystal mixture to align in a twisted-nematic configuration. The 50 μm cell gap is set by mixing silica spacers (Nippon Electrical Glass Co., Ltd) with an optical adhesive (Norland Optical Adhesive NOA 68). The glass cell is then placed under a UV lamp for 1 min to secure the two pieces together. Cell thickness is measured using an optical method based on the interference pattern of light internally reflected by the glass substrates in each empty cell.

2.2. LCE processing

LCEs are prepared using 1,4-bis-[4-(6-acryloyloxyhexyloxy) benzoyloxy]-2-methylbenzene (RM82) (Wilshire Technologies, Inc) as the monomer, *n*-butylamine (Sigma-Aldrich) as the chain extender, Irgacure I-369 (Sigma-Aldrich) as the photoinitiator, and VULCAN XC72 carbon black (Cabot Corporation) as the light absorbing particles. RM82 and *n*-butylamine are mixed in a 1.25 : 1 molar ratio to achieve the desired elasticity[36] with 1 wt% I-369 and 0.3 wt% carbon black. The mixture is heated to 110 °C and vortex-mixed for several cycles until the mixture is homogeneous. A twisted-nematic glass cell is filled with the mixture through capillary action and placed in a 75 °C oven for 12 h to oligomerize. The oligomerized mixture within the cell is then polymerized under 20 mW cm^{-2} intensity UV light with a wavelength of 365 nm (Thorlabs M365L2-C1) controlled with an LED driver (Thorlabs LEDD1B) for 30 min.

To validate monomer-to-polymer conversion, real-time infrared (RTIR) spectra are compared for the carbon black-embedded LCE mixture. Fig. S1 (ESI†) details the conversion of the acrylate group of the LCE mixture during polymerization. Fig. S2 (ESI†) provides conversion information determined by quantifying the decrease in peak area (eqn (S1), ESI†) for two characteristic peaks at 810 cm^{-1} and 1635 cm^{-1} that correspond to the carbon–carbon double bond in the acrylate moiety. LCE films reach conversion values of 80–90%, which indicates sufficient monomer conversion.

2.3. Computing LCE fabrication

Following polymerization, each glass cell is separated by wedging a razor blade in the cell gap. The LCE will remain laminated to one side of the cell, Fig. 1(d). For consistency, the LCEs are laminated to the side of the cell that has an alignment layer along the width of the glass piece. The LCE is then covered with 150 μm thick Kapton tape in preparation for laser-cutting the combinational logic pattern. Laser-cutting patterns are created with a computer-aided design (CAD) software SOLIDWORKS 2020 as a two-dimensional part. The color-coding feature is used to enable laser-cutting with various parameters in one pass. The laser cutter (Epilog Mini 24) is set to 12% power/35% speed for the switches and 8% power/30% speed for the trace pattern. These parameters enable the trace pattern to only cut through the tape layer, while the switch pattern is cut through both the tape layer and the LCE. The tape layer corresponding to the trace pattern is removed with tweezers and the exposed LCE is covered with a layer of ELMNT blade coating ink (donated by UES, Inc.). The ink is allowed to air-dry at room temperature for 6 h, upon which the remaining Kapton tape is carefully removed from the LCE. The conductive ink is a proprietary mixture of polymerized liquid metal networks (PolyLMN),[37,38] primarily composed of eutectic gallium indium (EGaIn) particles and 1-hexanol. Flexible conductor materials containing EGaIn are compatible with elastomeric substrates such as LCEs.[39] PolyLMN must be activated to facilitate a percolating network, which is commonly induced by stretching the host substrate since PolyLMN can undergo at least 744% strain.[38] Here, LCEs are not intended to be subjected to large strain, thus PolyLMN activation is achieved by applying a concentrated pressure along the trace. Following the blade-coating procedure, the computing LCE is then delaminated from the glass piece and adhered to a silicone substrate. This silicone substrate provides durability to the LCE film when wires are connected to the LED output display. At this point in the fabrication process, the LCE with integrated logic gates is complete and can be prepared for experimental validation.

2.4. Preparation for experimental testing

The silicone mold designs are created in SOLIDWORKS 2020 and sized to the same dimensions as the glass slide with a 10 mm depth and three-dimensionally (3D) printed (FlashForge Creator Pro) with acrylonitrile butadiene styrene (ABS). Liquid silicone (Smooth-On Dragon Skin 10 Slow) is mixed in a 1 : 1 ratio of A and B parts by hand for 3 min. The liquid silicone mixture is poured into each mold and allowed to cure for 4 h. The LCE film is then delaminated from the glass piece and adhered to the silicone substrate using a silicone adhesive (DAP All-Purpose) and allowed to dry for 12 h.

The enamel layer is removed from each end of enamel-coated copper wires (26 gauge) and is poked through the silicone and LCE layers to facilitate connection of the conductive traces to the LED output display. The LED output displays are designed as a multi-part CAD model and 3D printed with ABS. Three white LED diodes are secured into place behind each LED spot in pre-designated slots. A 9 V power supply is connected to the V_{CC} terminal in each computing LCE and is used to power the lights in the LED output display.

Barcode mask patterns are designed in SOLIDWORKS 2020 as a two-dimensional CAD and laser-cut from 1/32″ FR4 sheet. The laser cutter is set to 25% power/75% speed and required 10 passes to cut through the FR4 sheet.

In experiments, the barcode mask rests 1 cm above the LCE surface. AND and NAND logic gates are actuated with two UV LEDs (OmniCure LED UV MAX short head 365 nm with 6 mm focusing lens) and LED controller (OmniCure LX500) with a

total intensity of 200 mW cm^{-2}, while the 2-bit adder is actuated with a larger spot size UV LED (OmniCure AC8150P-HD-365 LED with custom collimator) controlled with a custom software (Hamilton's Venus Software) at 330 mW cm^{-2}. In switching characterization experiments, the NOT switches are actuated with a UV LED (Thorlabs M365L2-C1) and LED driver (Thorlabs LEDD1B) with an intensity of 50 mW cm^{-2}. Surface temperature of the LCEs is measured with an infrared thermometer (ETEKCITY Lasergrip 774). The surface temperature readings ensure LCE actuation occurs as a result of the photothermal effect, rather than heat emitted from the UV lights (Section S1.3, ESI†).

3. Results and discussion

3.1. Working principle of 1-bit switches

Buffer and NOT switches are the foundational 1-bit switching elements to compose any combinational logic operation.[20] Here, the photoresponsive LCE comprises unit cells containing either a Buffer or NOT switch. The LCE receives an optical signal, which is transformed to thermal energy, and locally triggers the curling actuation behavior. These switches connect and disconnect the conductive traces coated on the LCE surface, thus closing and opening the conductive pathway, respectively. Choosing PolyLMN as the conductive ink in this application is advantageous to ensure proper contact of the trace as the switch opens and closes. Upon activation, the oxide shell of encapsulated EGaIn particles in the PolyLMN breaks and the liquid metal flows slightly. This flow, while minimal, is sufficient to create an overlap of the trace at the interface between the switch tip and surrounding LCE film to maintain a percolating network across the entire conductive pathway over many cycles. A closed conductive pathway outputs an electrical digital signal that is visually represented in the LED displays for each computing LCE. An input of 1 denotes UV light irradiation, while an input of 0 refers to an absence of light. An output of 0 means the conductive pathway has been disconnected, while an output of 1 means the circuit is closed and the LED spot turns on. As shown in Fig. 1(c), a Buffer switch refers to a switch that exhibits the same output as the input, that is, a binary input, A, of 0 into the system results in a binary output, Q_B, of 0, while an input of 1 into the system results in an output of 1. The output of a NOT switch is opposite of the input, such that a binary input, A, of 0 results in an output, Q_N, of 1 and *vice versa*.

These switches can be combined to create an n-bit material system with 2^n configurations, denoted by the corresponding truth table to each individual logic operation. In n-bit materials, the unit cells are arranged in a matrix, where the columns are electrically connected in parallel and n rows are connected in series. Each material column corresponds to individual minterms in the Boolean function, while the rows correspond to individual inputs to the system.

In this material system, Buffer and NOT switches are achieved through the distinct polymerization temperatures of LCEs, as designated in Fig. 1(c). The Buffer switch is polymerized at an elevated temperature of 93 °C, while the NOT switch is polymerized at room temperature, 22 °C. Since this elevated temperature of 93 °C remains below the LCE nematic to isotropic transition temperature (T_{NI}) of 105 °C, the liquid crystals retain order. It has been shown experimentally that the polymerization temperature sets the temperature at which the LCE will be flat.[40,41] Thus, a Buffer switch in a twisted-nematic LCE polymerized at 93 °C will be curled at room temperature and flatten at elevated temperatures near the polymerization temperature. A NOT switch will start flat at room temperature and curl at elevated temperatures. Here, carbon black embedded in the polymer network is used to enact the photothermal effect as a result of the carbon black particles absorbing UV light and producing local heat.

It is important to note that Buffer and NOT switches are oriented orthogonally relative to each other. The Buffer switch is oriented parallel to the alignment layer of the bottom glass piece, while the NOT switch is oriented perpendicular. In an ordinary twisted-nematic LCE, one would expect curling behavior that aligns with the behavior of the NOT switch, where the deflection is orthogonal to the alignment of the bottom surface of the LCE. Conversely, a Buffer switch curls in the opposite direction such that the deflection is parallel to the alignment of the bottom surface of the LCE. This opposing behavior is caused by the anisotropic thermal expansion of liquid crystals in LCEs.

The Buffer and NOT switches incorporate a tapered geometry to enhance switching rate and consistency. This concept draws from mechanics, where a tapered geometry for a cantilever beam with a tip mass limits stress concentration at the fixed end and enables a larger power output.[42] We can relate the switches in this study to a cantilever beam with a distributed mass, as the conductive trace spans the entire length of the switch. Despite inherent distinctions between the two systems, the adoption of a tapered geometry remains advantageous. This approach harnesses potential benefits regarding the mechanics of the switch, while concurrently reducing contact area between the LCE film and switch tip. Laser-cutting as a fabrication technique yields irregular edges, which can cause the LCE to get caught on itself, thus minimizing contact area at the interface is favorable.

3.2. Switching rate characterization

For practical use, the optomechanical computing LCE system must have a sufficiently fast actuation speed. The switching rates for six switch geometries are characterized, among which five of the six switches have a tip width (w) that is scaled as a factor of the width of the conductive trace. A conductive trace width of 600 μm and thickness of 150 μm is found to lend a sufficient amount of PolyLMN to ensure a percolating network throughout the logic gate circuitry. Thus, switches with a tip width of 0.6 mm, 1.2 mm, 1.8 mm, 2.4 mm, 3.0 mm, and 3.5 mm are studied. The widest tip at 3.5 mm is chosen to compare a rectangular shape to the tapered geometry. The height, h, and base, b, dimensions of all switches in this study are 3.75 mm and 3.5 mm, respectively. These dimensions

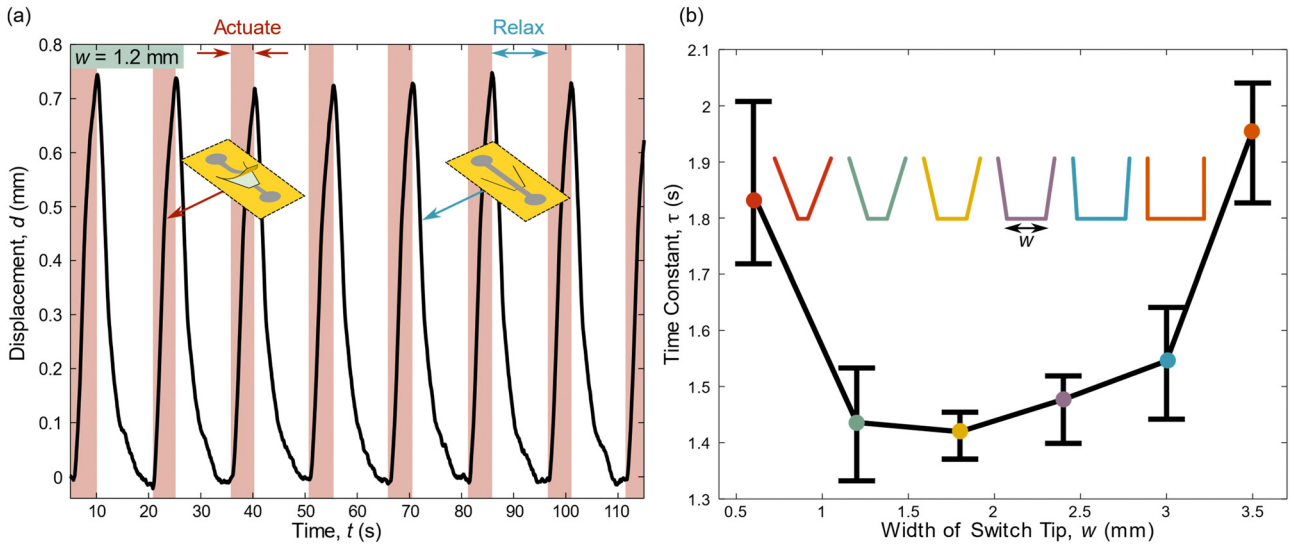

Fig. 2 (a) Displacement time series of a NOT switch with a 1.2 mm tip width through actuation and relaxation cycles. (b) Comparison of six tapered and rectangular switch geometries to study differences in switching rate. Time constant values are derived from the displacement time series during the actuation periods. Reported data points represent the mean time constant value, τ_{avg}, and error bars represent the range from minimum to maximum time constant values, τ_{min} and τ_{max}.

provide a sufficient aspect ratio that allows the switch to deflect consistently in response to a broad range of light intensities. The NOT switches are chosen to characterize the switching rate since all NOT switch geometries begin in a similar planar configuration. A laser displacement sensor captures deflection of the switch over time as the UV light turns on and off in 5 and 10 s intervals, respectively. A schematic representation of the laser displacement measurement is provided in Fig. S3 (ESI†). The switch is allotted a relaxation period longer than the actuation period since it was found that the LCE takes longer to fully relax than to actuate with the UV intensity setting used in measurements. Time to actuate and relax can be modified by altering switch geometry, carbon black concentration, and UV intensity.[43]

Fig. 2(a) shows the displacement in time of a switch with w = 1.2 mm. The actuation and relaxation periods of the switch are observed as a result of cyclic UV light exposures. Similar data collection is performed for all six uniquely dimensioned switches. The switch tip displacement d is fit with a curve of the form $d = ae^{-t/\tau}$. The average time constant, τ, values are derived from these curves and represented in Fig. 2(b) to demonstrate variation in switching rate among the selected switch geometries.

The switch with the smallest time constant of 1.42 s and thus fastest switching rate is the switch with w = 1.6 mm. The percent difference between time constant values for w = 1.6 mm and w = 3.0 mm switches is 8.6%. As a result, the variation of tip width of switches with a tapered geometry within the range of 1.2–3.0 mm has minimal impact. Further, the switch with a tip width equal to the width of the conductive trace has a time constant value of 1.84 s. This switch is only slightly faster than the rectangular switch with w = 3.5 mm, which has a time constant of 1.96 s. From these results, a percent difference of 25.8% between switches with w = 0.6 mm and w = 1.6 mm indicates that a tapered geometry enables faster switching, provided the tip width is greater than the conductive trace.

3.3. Proof of concept LCEs with integrated logic gates

AND and NAND logic gates are demonstrated to realize implementation of Buffer and NOT switches in 2-bit materials. AND and NAND logic gates are two of six fundamental 2-bit logic gates that comprise all combinational logic sequences. The AND gate, shown in Fig. 3(a), consists of two Buffer switches connected in series, while the NAND gate, shown in Fig. 3(b), is created with two NOT switches in parallel. The AND and NAND logic gates are fabricated similar to individual Buffer and NOT switches, where the AND LCE is polymerized at an elevated temperature and the NAND LCE is polymerized at room temperature.

Following the fabrication of the logic gate samples, the experiments use a UV light and barcode mask to progress through each step of the corresponding truth tables. The two 1-bit inputs A and B correspond to strips of light in the barcode. The barcode mask is altered for each corresponding input in the truth table, blocking a strip of light when the input is 0, and allowing light to pass through and irradiate the sample when the input is 1. When the UV light is turned on, the irradiated switches move to the "on" position for a Buffer and the "off" position for a NOT. Each logic gate has a single 1-bit output, Q_{AND} and Q_{NAND}, that is connected to the LED output display with enamel wires. The LED output display serves as a visual depiction of the binary signals, both high and low, transmitted from the computing LCE. In this context, a low signal of 0 correlates with a LED spot turned off, while a high signal of 1 corresponds to an illuminated LED spot. Experimental validation of the AND logic gate is shown in Fig. 3(c) and the NAND logic gate is shown in Fig. 3(d). Video footage of these behaviors is in Video S1 (ESI†). These 2-bit logic gates demonstrate the

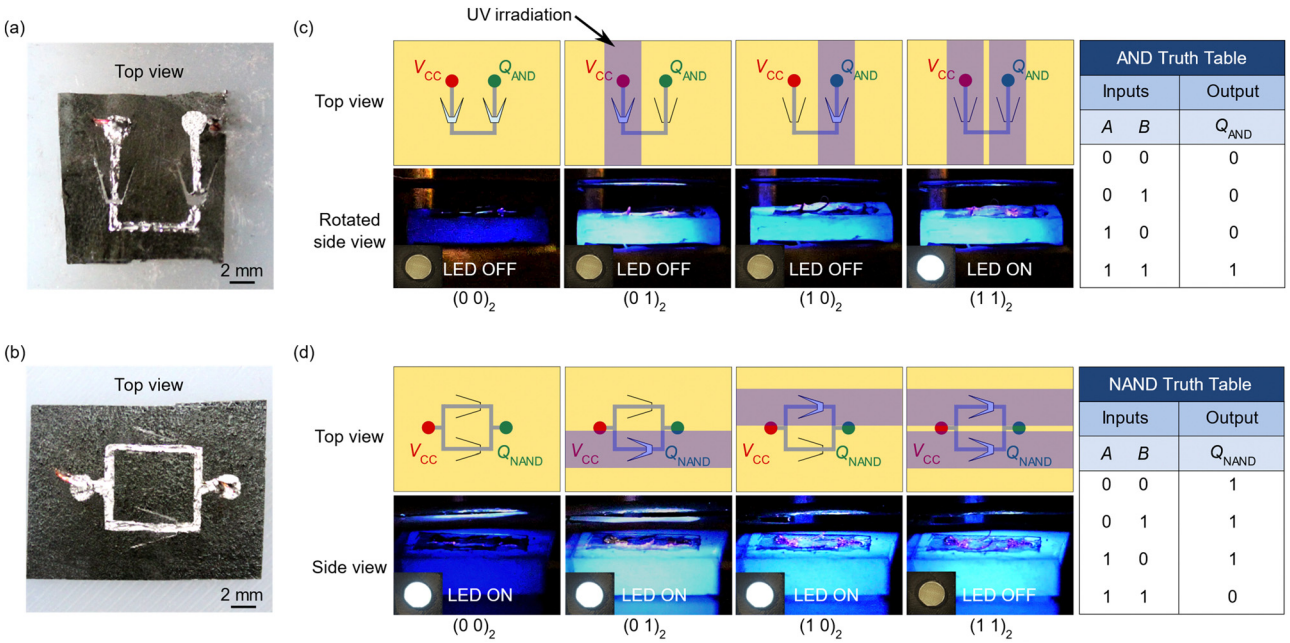

Fig. 3 Experimental image of photoresponsive LCEs with integrated (a) AND and (b) NAND logic gates. Each possible configuration in the corresponding (c) AND and (d) NAND truth tables are represented schematically and experimentally. The top view schematic displays barcode-patterned UV irradiation for each configuration, as indicated by the inputs in the truth table. An input of 1 indicates UV irradiation, while an input of 0 indicates no UV irradiation. The LED light corresponds to the output value in the truth table, where "on" is an output of 1 and "off" is an output of 0.

capability to network independent Buffer and NOT switches into higher-level combinational logic sequences.

3.4. Scalable optomechanical computing in photoresponsive LCEs

Scaling up from simple logic gates containing Buffer and NOT switches to combinational logic-based integrated circuits requires an additional fabrication step, detailed in Fig. 4(a).

Here, a pixelated photomask is created to expose regions of the LCE that will be polymerized at an elevated temperature, namely the Buffer switches. The Buffer and NOT switches are designed to fit into a square pixel, such that any combinational logic operation can be patterned in a grid. Following selective polymerization of the LCE in regions where the Buffer switches are located, the LCE is removed from the hot plate and reaches room temperature after 10 min. The remaining areas of the LCE

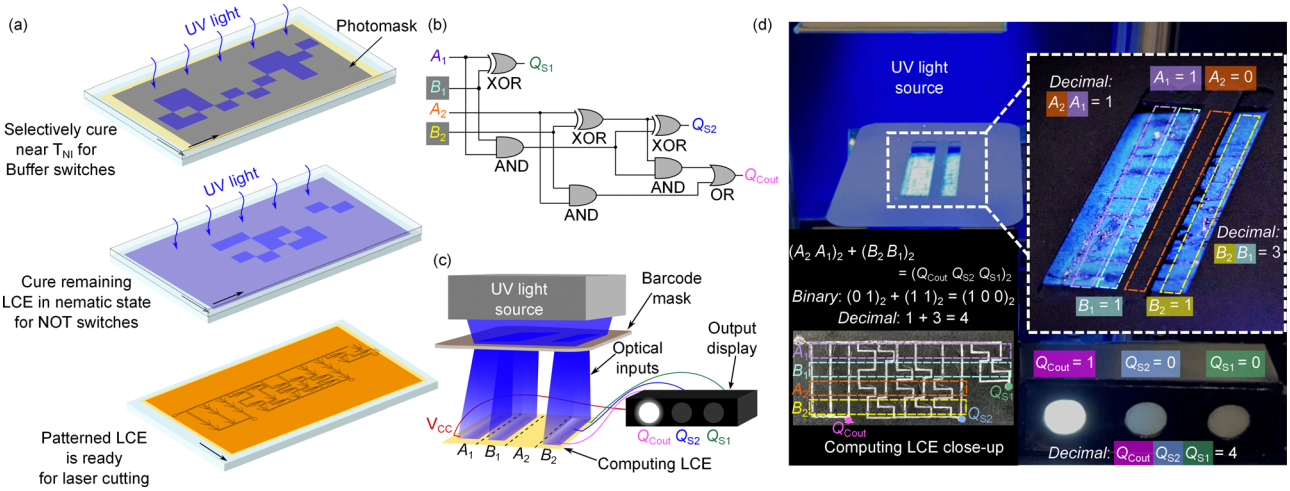

Fig. 4 (a) Additional fabrication step to incorporate Buffer and NOT switches in a single LCE film *via* selective polymerization. (b) Logic gate diagram for a 2-bit adder. (c) Schematic of experimental setup for the 2-bit adder LCE. Optical information is patterned with the barcode mask and processed by the computing LCE. Based on the conductive pathways, a digital signal (or lack thereof) is visualized in the LED output display. This particular combination of inputs and outputs correspond to a single configuration in the 2-bit adder truth table. (d) Experimental image of the equivalent setup described in part (c). Binary and decimal values to correspond to the chosen configuration are provided as well as experimental images of the 2-bit adder LCE with and without irradiation.

are polymerized, and the same procedure described in Section 3.1 is followed to complete the fabrication process.

In this study, a 2-bit adder is chosen to demonstrate the versatility of these design and fabrication methods. The logic diagram of a 2-bit adder is found in Fig. 4(b). This particular computing LCE demonstrates arithmetic, though circuitry for other combinational logic operations can be incorporated in the material network because Buffer and NOT switches can be used to fashion any combinational logic integrated circuit.[20] A 2-bit adder is a combinational logic operation that adds two 2-bit numbers (A and B) together to a 3-bit sum (Q). The optical inputs correspond to two-digit binary numbers $(A_2\,A_1)_2$ and $(B_2\,B_1)_2$, and the digital outputs correspond to a three-digit binary number $(Q_{\mathrm{Cout}}\,Q_{\mathrm{S2}}\,Q_{\mathrm{S1}})_2$. Each output is integrated in the design of the material as its own section, such that closing a conductive pathway within any section lights up the corresponding LED spot in the output display.

The truth table for a specific logic operation can be deduced from the logic diagram, which is then used to generate the canonical Boolean function for each output in terms of only combinations of Buffer and NOT switches. In the case of the 2-bit adder, the Boolean function corresponds to a material system composed of 60 switches and 64 unit cells. El Helou *et al.*[20] detailed a methodology to reduce the number of switches required to achieve a higher computational density with use of the Quine-McCluskey (QM) algorithm.[44] The QM algorithm enables minimization of the canonical Boolean function while achieving the same computing functionality, and reduces the Boolean function for a 2-bit adder to 32 switches and 44 unit cells. In this material system, the switches are organized in 4 rows, representing the 4 binary value inputs, and 11 columns, with 8 switches in each row according to the minimized Boolean function (eqn (S2)–(S4), ESI†).

The experimental setup for the 2-bit adder is similar to that of the AND and NAND logic gates, where a barcode mask is set between the computing LCE and the UV light source, Fig. 4(c). This barcode mask has four rows, corresponding to the four 1-bit inputs, while the LED output display has three lights that account for the three binary output signals $(Q_{\mathrm{Cout}}\,Q_{\mathrm{S2}}\,Q_{\mathrm{S1}})_2$. One configuration from the 2-bit adder truth table is schematically shown in Fig. 4(c) with the experimental equivalent represented in Fig. 4(d). This particular configuration pertains to binary inputs $(A_2\,A_1)_2$ as $(0\,1)_2$ and $(B_2\,B_1)_2$ as $(1\,1)_2$, which corresponds to decimal numbers 1 and 3, respectively. These two numbers are added together to reach a decimal output of 4, which is represented by the binary number $(Q_{\mathrm{Cout}}\,Q_{\mathrm{S2}}\,Q_{\mathrm{S1}})_2$ as $(1\,0\,0)_2$. All possible configurations for the 2-bit adder and active conductive pathways for each configuration are schematically represented in Fig. S4 (ESI†). An experimental demonstration of the 2-bit adder through all 16 configurations is provided in Video S2 (ESI†). As observed in Video S2 (ESI†), this exemplary material decodes barcode-like optical signals into their numeric values, performs the arithmetic addition operation, and then displays a binary representation of the summation output. These capabilities are a result of the intrinsic material properties of carbon black-embedded LCEs coupled with the arrangement of 1-bit switches to realize a specific Boolean function.

Video S2 (ESI†) shows that there exist delays in the LED output display responses for certain input combinations. Parameters such as the switch geometry, UV intensity, and carbon black concentration contribute to the lag in response of the LED output display. Additionally, the larger range of variability in lag time for the 2-bit adder LCE is likely attributed to a nonuniform layer of PolyLMN on the surface of individual switches. While the LCEs are initially blade-coated with a uniform layer of PolyLMN, activation of the ink triggers the liquid metal to flow to a slight degree, leading to a nonuniform distribution of PolyLMN. Additionally, these nonuniformities can result in differing amounts of PolyLMN at the interface between the switch tip and surrounding LCE film, suggesting that switches with an increased amount of PolyLMN at the tip require the actuation force to be applied over a longer duration to overcome the adhesion force of PolyLMN to itself.

The material system presented here performs the addition of two numbers, though the framework has the potential to accomplish any combinational logic process. As a result, the optomechanical computing materials in this work can be utilized for arithmetic, comparators, decoders, or encoders. Additionally, the functions of these components could be combined to create material systems capable of high-level thought processes.

4. Conclusions

The development of optomechanical computing materials marks a significant leap forward in the development of soft, autonomous devices. The system demonstrated in this work highlights an optomechanical computing LCE film capable of receiving and processing optical information communicated *via* barcode-like digitized light signals. The concepts described in this report may also be employed for implementing a rudimentary sense of sight in soft robotic systems or for untethered operation in harsh conditions, such as satellites in orbit. This foundation for optically-based decision-making functionality in soft, engineered matter paves the path for embodied intelligence in material systems.

Author contributions

H. M. T. and R. L. H. designed the research; H. M. T. and C. P. A. fabricated samples; H. M. T. performed the research and experiments; H. M. T. and K. M. L. collected and analyzed data; H. M. T. and R. L. H. wrote the paper with edits to follow from C. P. A., K. M. L., and P. R. B.

Conflicts of interest

There are no conflicts to declare.

Acknowledgements

This research is supported in part by a National Science Foundation (NSF) Air Force Research Laboratory (AFRL) INTERN grant (CMMI-2217608), and funds from the Department of Mechanical Engineering at Penn State University. The authors would like to thank Dr. Michael McConney, Dr. Christopher Tabor, and Dr. Nicholas Godman of the Materials and Manufacturing Directorate at the Air Force Research Laboratory for use of lab space and equipment during the NSF AFRL INTERN program. The authors would also like to acknowledge Ecklin Crenshaw of the Air Force Research Laboratory for assistance with lab equipment and Dr. Charles El Helou of Penn State University for insightful conversations during this project.

References

1 M. Schwartz and J. P. F. Lagerwall, Embedding intelligence in materials for responsive built environment: A topical review on liquid crystal elastomer actuators and sensors, *Build. Environ.*, 2022, **226**, 109714.
2 M. Pishvar and R. L. Harne, Foundations for soft, smart matter by active mechanical metamaterials, *Adv. Sci.*, 2020, **7**, 2001384.
3 C. Majidi, Soft-matter engineering for soft robotics, *Adv. Mater. Technol.*, 2019, **4**, 1800477.
4 R. Pfeifer, F. Iida and M. Lungarella, Cognition from the bottom up: on biological inspiration, body morphology, and soft materials, *Trends Cognit. Sci.*, 2014, **18**, 404–413.
5 X. Song, A. Eshra, C. Dwyer and J. Reif, Renewable DNA seesaw logic circuits enabled by photoregulation of toehold-mediated strand displacement, *RSC Adv.*, 2017, **7**, 28130–28144.
6 C. D. Santangelo, Making smarter materials, *Nat. Mater.*, 2023, **22**, 3–4.
7 S. Furber, Large-scale neuromorphic computing systems, *J. Neural Eng.*, 2016, 13.
8 A. Steane, Quantum computing, *Rep. Prog. Phys.*, 1998, **61**, 117.
9 C. A. Aubin, B. Gorissen, E. Milana, P. R. Buskohl, N. Lazarus and G. A. Slipher, *et al.*, Towards enduring autonomous robots via embodied energy, *Nature*, 2022, **602**, 393–402.
10 C. Kaspar, B. J. Ravoo, W. G. van der Wiel, S. V. Wegner and W. H. P. Pernice, The rise of intelligent matter, *Nature*, 2021, **594**, 345–355.
11 M. A. McEvoy and N. Correll, Materials that couple sensing, actuation, computation, and communication, *Science*, 2015, **347**, 1261689.
12 C. El Helou, P. R. Buskohl, C. E. Tabor and R. L. Harne, Digital logic gates in soft, conductive mechanical metamaterials, *Nat. Commun.*, 2021, **12**, 1633.
13 D. J. Preston, P. Rothemund, H. J. Jiang, M. P. Nemitz, J. Rawson and Z. Suo, *et al.*, Digital logic for soft devices, *Proc. Natl. Acad. Sci. U. S. A.*, 2019, **116**, 7750–7759.
14 Y. Jin, Y. Lin, A. Kiani, I. D. Joshipura, M. Ge and M. D. Dickey, Materials tactile logic via innervated soft thermochromic elastomers, *Nat. Commun.*, 2019, **10**, 4187.
15 Z. Wang, X. Zhang, Y. Wang, Z. Fang, H. Jiang and Q. Yang, *et al.*, Untethered Soft Microrobots with Adaptive Logic Gates, *Adv. Sci.*, 2023, **10**, 2206662.
16 Y. Jiang, L. M. Korpas and J. R. Raney, Bifurcation-based embodied logic and autonomous actuation, *Nat. Commun.*, 2019, **10**, 128.
17 H. Komatsu, S. Matsumoto, S. Tamaru, K. Kaneko, M. Ikeda and I. Hamachi, Supramolecular hydrogel exhibiting four basic logic gate functions to fine-tune substance release, *J. Am. Chem. Soc.*, 2009, **131**, 5580–5585.
18 X. Xia, C. M. Spadaccini and J. R. Greer, Responsive materials architected in space and time, *Nat. Rev. Mater.*, 2022, **7**, 683–701.
19 H. Yasuda, P. R. Buskohl, A. Gillman, T. D. Murphey, S. Stepney and R. A. Vaia, *et al.*, Mechanical computing, *Nature*, 2021, **598**, 39–48.
20 C. El Helou, B. Grossmann, C. E. Tabor, P. R. Buskohl and R. L. Harne, Mechanical integrated circuit materials, *Nature*, 2022, **608**, 699–703.
21 S. I. Rich, R. J. Wood and C. Majidi, Untethered soft robotics, *Nat. Electron.*, 2018, **1**, 102–112.
22 S. J. Park, M. Gazzola, K. S. Park, S. Park, V. Di Santo and E. L. Blevins, *et al.*, Phototactic guidance of a tissue-engineered soft-robotic ray, *Science*, 2016, **353**, 158–162.
23 R. L. Truby, Designing soft robots as robotic materials, *Acc. Mater. Res.*, 2021, **2**, 854–857.
24 W. Wang, Y. Wang, H. Bao, B. Xiong and M. Bao, Friction and wear properties in MEMS, *Sens. Actuators, A*, 2002, **97–98**, 486–491.
25 J. W. Chung, S. J. Yoon, S. J. Lim, B. K. An and S. Y. Park, Dual-mode switching in highly fluorescent organogels: binary logic gates with optical/thermal inputs, *Angew. Chem., Int. Ed.*, 2009, **48**, 7030–7034.
26 Y. Shi, H. Sun, J. Xiang, H. Chen, Q. Yang and A. Guan, *et al.*, Construction of DNA logic gates utilizing a H^+/Ag^+ induced i-motif structure, *Chem. Commun.*, 2014, **50**, 15385–15388.
27 T. J. White and D. J. Broer, Programmable and adaptive mechanics with liquid crystal polymer networks and elastomers, *Nat. Mater.*, 2015, **14**, 1087–1098.
28 G. E. Bauman, J. D. Hoang, M. F. Toney and T. J. White, Degree of orientation in liquid crystalline elastomers defines the magnitude and rate of actuation, *ACS Macro Lett.*, 2023, **12**, 248–254.
29 K. M. Herbert, H. E. Fowler, J. M. McCracken, K. R. Schlafmann, J. A. Koch and T. J. White, Synthesis and alignment of liquid crystalline elastomers, *Nat. Rev. Mater.*, 2022, **7**, 23–38.
30 M. Warner, Topographic mechanics and applications of liquid crystalline solids, *Annu. Rev. Condens. Matter Phys.*, 2020, **11**, 125–145.
31 Z. Zhang, V. P. Panov, M. Nagaraj, R. J. Mandle, J. W. Goodby and G. R. Luckhurst, *et al.*, Raman scattering studies of order parameters in liquid crystalline dimers exhibiting the nematic and twist-bend nematic phases, *J. Mater. Chem. C*, 2015, **3**, 10007–10016.

32 K. M. Lee, T. J. Bunning and T. J. White, Autonomous, hands-free shape memory in glassy, liquid crystalline polymer networks, *Adv. Mater.*, 2012, **24**, 2839–2843.
33 F. Pujol-Vila, P. Güell-Grau, J. Nogués, M. Alvarez and B. Sepúlveda, Soft optomechanical systems for sensing, modulation, and actuation, *Adv. Funct. Mater.*, 2023, **33**, 2213109.
34 Y. Yu, M. Nakano and T. Ikeda, Directed bending of a polymer film by light, *Nature*, 2003, **425**, 145.
35 S. Tasmim, Z. Yousuf, F. S. Rahman, E. Seelig, A. J. Clevenger and S. N. VandenHeuvel, *et al.*, Liquid crystal elastomer based dynamic device for urethral support: Potential treatment for stress urinary incontinence, *Biomaterials*, 2023, **292**, 121912.
36 T. H. Ware and T. J. White, Programmed liquid crystal elastomers with tunable actuation strain, *Polym. Chem.*, 2015, **6**, 4835–4844.
37 M. D. Dickey, Stretchable and soft electronics using liquid metals, *Adv. Mater.*, 2017, **29**, 1606425.
38 C. J. Thrasher, Z. J. Farrell, N. J. Morris, C. L. Willey and C. E. Tabor, Mechanoresponsive polymerized liquid metal networks, *Adv. Mater.*, 2019, **31**, 1903864.
39 J. Sgotti Veiga, M. Reis Carneiro, R. Molter, M. Vinciguerra, L. Yao and C. Majidi, *et al.*, Toward fully printed soft actuators: UV-assisted printing of liquid crystal elastomers and biphasic liquid metal conductors, *Adv. Mater. Technol.*, 2023, 2300144.
40 J. J. Wie, K. M. Lee, T. H. Ware and T. J. White, Twists and turns in glassy, liquid crystalline polymer networks, *Macromolecules*, 2015, **48**, 1087–1092.
41 H. Kim, J. Gibson, J. Maeng, M. O. Saed, K. Pimentel and R. T. Rihani, *et al.*, Responsive, 3D electronics enabled by liquid crystal elastomer substrates, *ACS Appl. Mater. Interfaces*, 2019, **11**, 19506–19513.
42 W. Cai and R. L. Harne, Vibration energy harvesters with optimized geometry, design, and nonlinearity for robust direct current power delivery, *Smart Mater. Struct.*, 2019, **28**, 075040.
43 J. Shin, J. Sung, M. Kang, X. Xie, B. Lee and K. M. Lee, *et al.*, Light-triggered thermal conductivity switching in azobenzene polymers, *Proc. Natl. Acad. Sci. U. S. A.*, 2019, **116**, 5973–5978.
44 E. J. McCluskey, Minimization of Boolean functions, *Bell Syst. Tech. J.*, 1956, **35**, 1417–1444.

